Supporting Information

Integrating Atomic Scale Catalyst Design with Transport Engineering for Stable and Efficient CO_2 Electrolysis to CO in a Membrane Electrode Assembly

Zahra Teimouri,[1] Mahtab Masouminia,[1] Ashkan Irannezhad,[1] Reza Eslami,[1] Joseph Deering,[2] Navid Noor,[1] Shunquan Tan,[1] Amirhossein Foroozan Ebrahimy,[1] Shayan Angizi,[1] Sung-Fu Hung,[3] and Drew Higgins [1,*]

[1]*Department of Chemical Engineering, McMaster University, Hamilton, ON, Canada*

[2] *Canadian Center for Electron Microscopy, Hamilton, ON, Canada*

[3] *Department of Applied Chemistry and Center for Emergent Functional Matter Science, National Yang Ming Chiao Tung University, Hsinchu 300, Taiwan*

**higgid2@mcmmaster.ca*

Table of Contents

Table S1. Comparison of CO_2R performance and stability of NiNCNT-sim 800 °C with state-of-the-art NiNC and Ag catalysts in MEA.

Catalyst	Cell voltage (V)	j_{co} (mA cm^{-2})	j_{total} (mA cm^{-2})	EE (%)	TOF** (s^{-1})	Stability	Reference
0.69*NiNCNT-sim 800 °C	**3.2**	**558.4**	**607.4**	**39.2**	**0.26**	**210 h at 100 mA cm^{-2}**	**This work**
3.02 NiNCNT	2.4	225.2	300.2	36.3	0.01	70 h at 100 mA cm^{-2}	(1)
AlNC (ZIF-based)	3.6	644.1	700.3	30.5	0.36	17 h at 100 mA cm^{-2}	(2)
0.27NiNCB	2.7	132.2	137.5	47.6	0.03	20 h at 100 mA cm^{-2}	(3)
1.5NiNCB	3.1	176.1	195.5	38.9	0.1	8 h (at H-cell, -0.9 V vs RHE)	(4)
1.5NiNCNT	3.0	156.9	162.5	41.0	0.09	8 h (at H-cell, -0.9 V vs RHE)	(4)
1.5NiNBiochar	2.9	170.0	191.0	41.1	0.09	8 h (at H-cell, -0.9 V vs RHE)	(4)
4.3NiNCB	3.5	510.5	566.6	34.4	0.02	10 h at 360 mA cm^{-2}	(5)
3NiNGS	3.0	460.2	567.9	36.1	0.13	N.A.	(6)
1.6NiNPC	3.2	225.7	250.2	37.6	0.14	73 h at 225 mA cm^{-2}	(7)
Ag-NB-NW	3.6	475.2	500.2	35.3	N.A.	240 h at 400 mA cm^{-2}	(8)
Ag NPs	3.2	466.1	517.8	37.6	N.A.	200 h at 420 mA cm^{-2}	(9)
Ag NPs	3.5	100.1	105.2	36.3	N.A.	1000 h at 100 mA cm^{-2}	(10)
Ag NPs/PipierION	3.1	100.2	125.1	34.5	N.A.	200 h at 100 mA cm^{-2}	(11)
Ag NPs	4.8	300.1	428.6	19.5	N.A.	1200 h at 300 mA cm^{-2}	(12)
Ag-SiO_2	3.5	700.1	823.6	32.5	N.A.	12 h at 700 mA cm^{-2}	(13)

* Nominal Ni loading in wt.%

** As TOF is a function of cell voltage, only values obtained at similar voltages should be interpreted and compared. TOF values are not reported for Ag-based catalysts due to the lack of available information on electrochemically active surface area and site density required for reliable normalization.

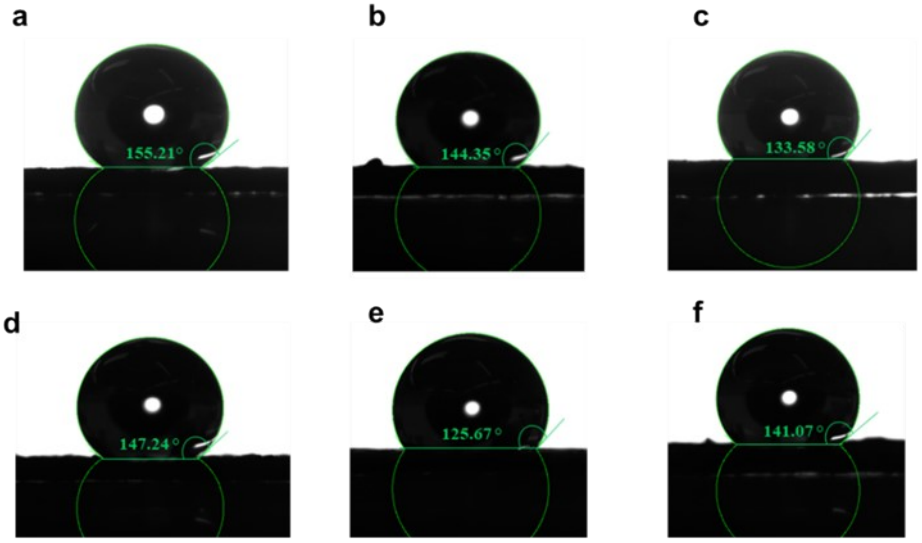

Fig. S1 | Contact angle measurements on the **a,** NiNCNT-sim 700 °C, **b,** NiNCNT-sim 800 °C, **c,** NiNCNT-sim 900 °C, **d,** NiNCNT-phys 700 °C, **e,** NiNCNT-phys 800 °C, and **f,** NiNCNT-phys 900 °C.

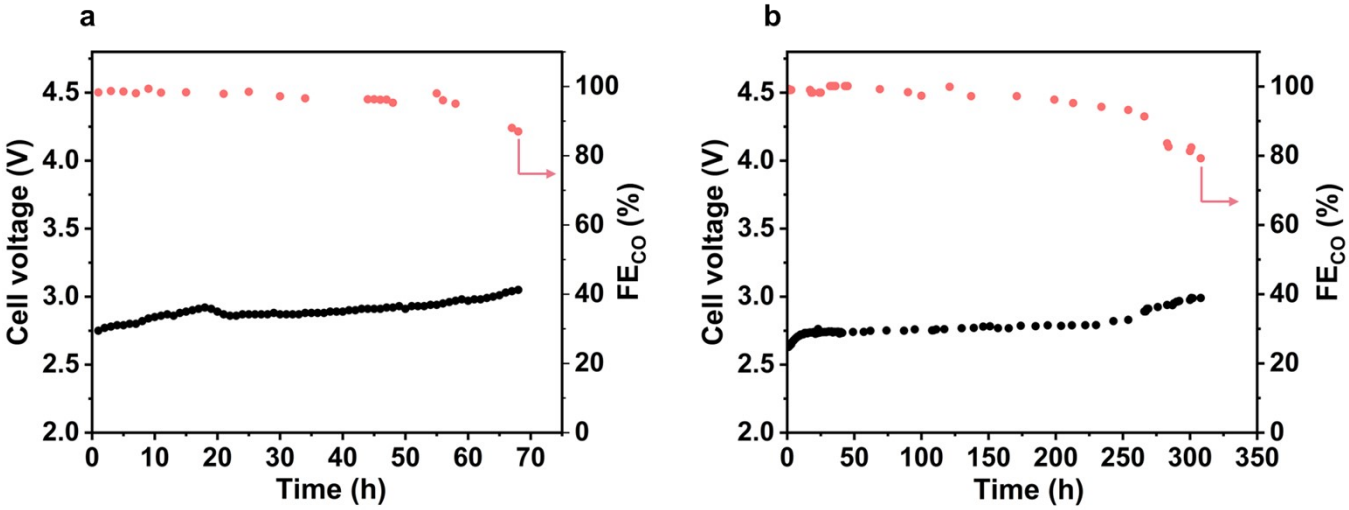

Fig. S2 | Stability of the NiNCNT-sim 800 °C electrode in a MEA under pulsed chronopotentiometry conditions (3 s at applied current density and 1 s at 0 mA cm^{-2}) using 0.1M $KHCO_3$ electrolyte: **a,** 200 mA cm^{-2}, **b,** 100 mA cm^{-2}.

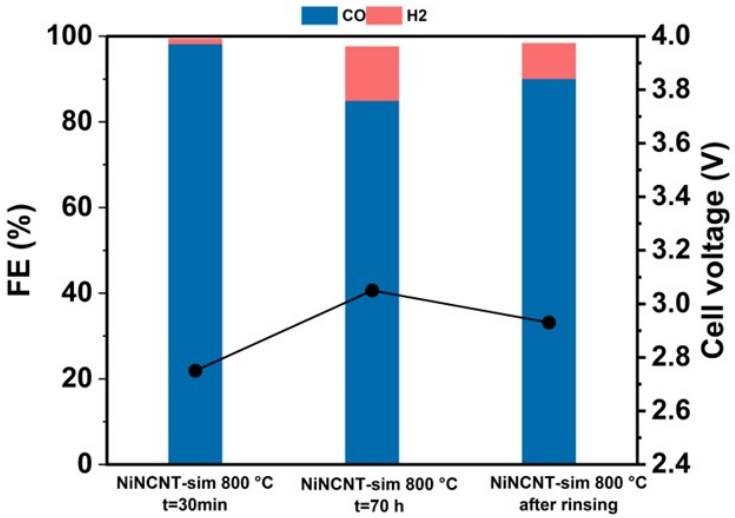

Fig. S3 | CO_2R performances of NiNCNT-sim 800 °C electrode after 30 minutes of pulse chronopotentiometry (3s at 200 mA cm^{-2}, 1s at 0 mA cm^{-2}), NiNCNT-sim 800 °C electrode after 70 hours of pulse chronopotentiometry, and NiNCNT-sim 800 °C electrode after 70 hours of pulse chronopotentiometry, and rinsed with water to remove salt precipitations followed by drying. All tests were performed in a MEA, using 0.1M $KHCO_3$ anolyte.

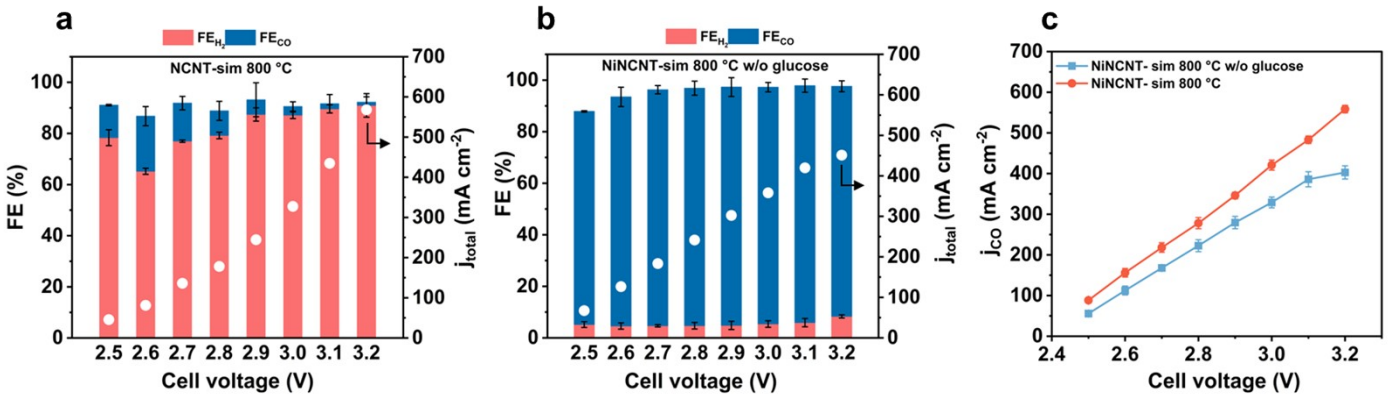

Fig. S4 | CO_2R performances of **a,** NCNT-sim 800 °C, **b,** NiNCNT-sim 800 °C w/o glucose and **c,** CO partial current density of NiNCNT-sim 800 °C with and without glucose. The error bars in **a** and **b,** correspond to the standard deviation of three independent measurements.

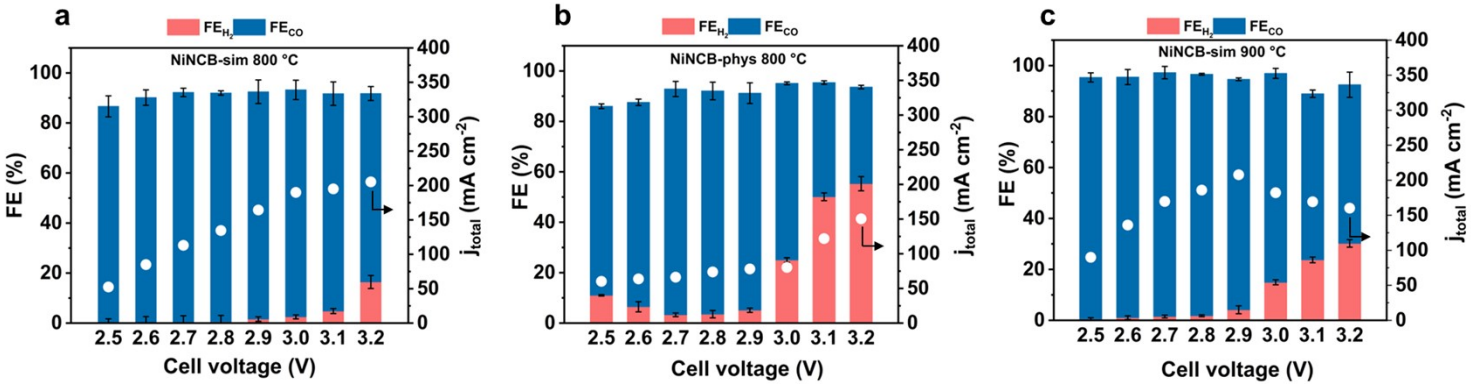

Fig. S5 | CO_2R performances of **a,** NiNCB-sim 800 °C, and **b,** NiNCB-phys 800 °C, and **c,** NiNCB-sim 900 °C electrodes. The error bars in **a-c**, correspond to the standard deviation of three independent measurements.

Table S2. BET results for the synthesized catalysts.

Catalyst	BET surface area ($m^2.g^{-1}$)	Pore volume ($cm^3.g^{-1}$)	Micropore area* ($m^2.g^{-1}$)	Mesopore area* ($m^2.g^{-1}$)
Acid-treated CB	758	1.03	537	221
Acid-treated CNT	486	1.47	119	367
NiNCNT-phys 700 °C	165	0.52	32	149
NiNCNT-phys 800 °C	373	0.87	115	258
NiNCNT-phys 900 °C	472	1.38	98	373
NiNCNT-sim 700 °C	218	0.74	32	149
NiNCNT-sim 800 °C	596	1.38	159	436
NiNCNT-sim 900 °C	422	1.15	83	338
NiNCNT-sim 800 °C-w/o glucose	539	1.41	129	409
NiNCB-phys 800 °C	645	0.88	426	218
NiNCB-sim 800 °C	1019	1.43	535	510
NiNCB-sim 900 °C	1034	1.45	469	526

* Micropore area corresponds to pores with diameters <2 nm, while mesopore area refers to pores between 2–50 nm in diameter. Values were calculated using Quenched Solid Density Functional Theory (QSDFT) modeling, assuming slit/cylindrical pore geometry for CNT-derived catalysts and slit pores for CB-based catalysts.

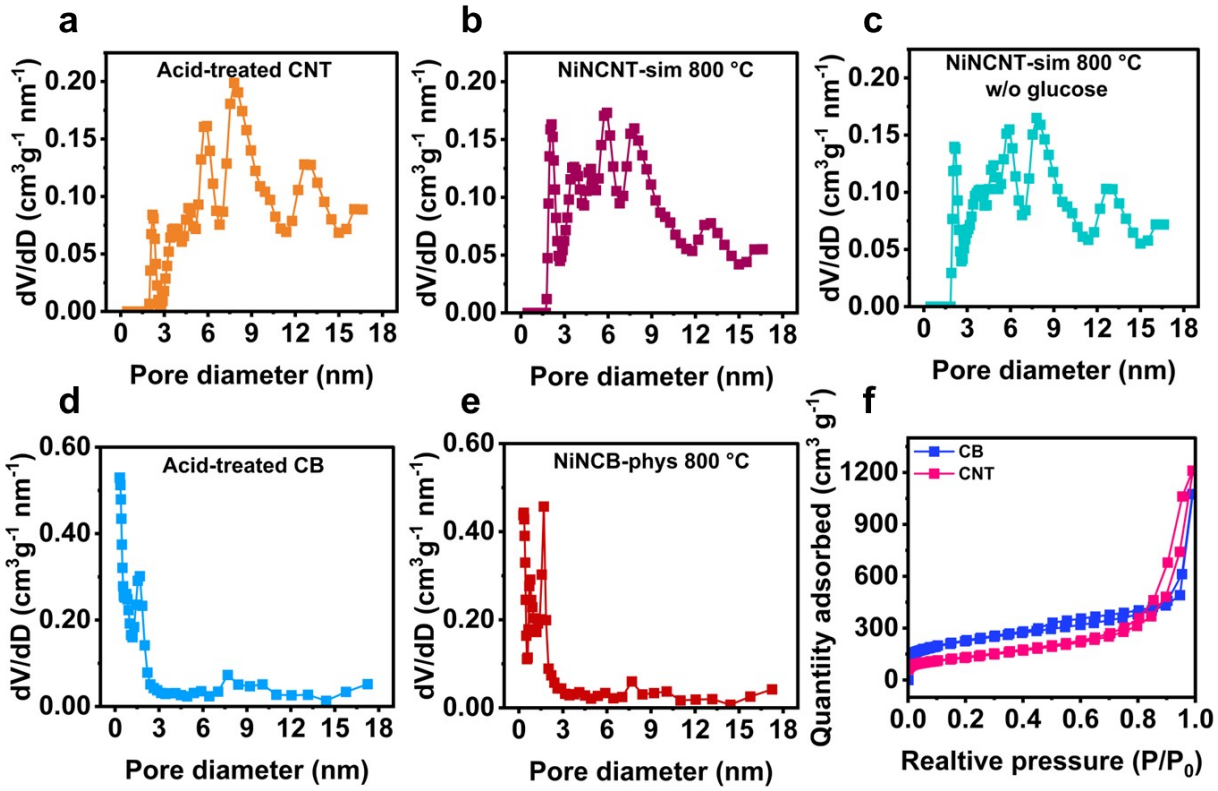

Fig. S6 | Pore size distributions of **a,** acid-treated CNTs, **b,** NiNCNT-sim 800 °C, **c,** NiNCNT-sim 800 °C w/o glucose, **d,** pore size distribution of acid-treated CB, **e,** NiNCB-phys 800 °C, and **f,** N_2 sorption isotherms of acid-treated CNT and CB.

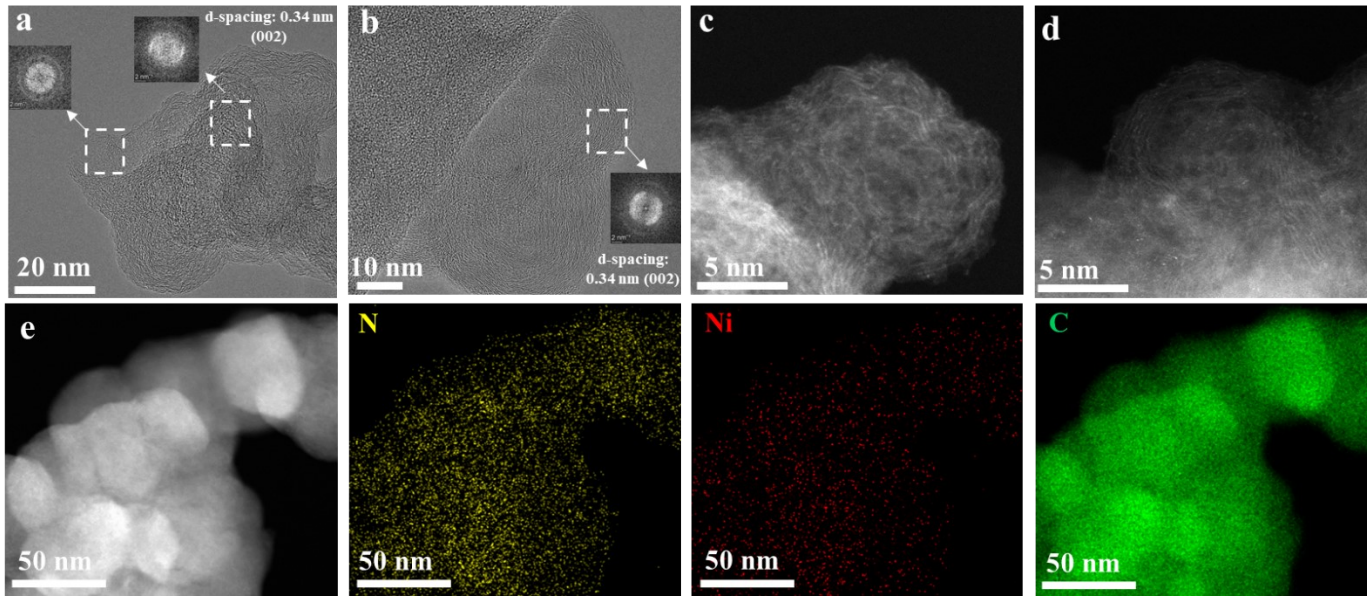

Fig. S7 | a, HRTEM image of NiNCB-sim 800 °C **b,** HRTEM image of acid-treated CB **c, d,** HAADF-STEM images showing atomically dispersed Ni species in NiNCB-sim 800 °C. and **e,** Elemental mapping (EDX) confirming uniform distribution of C, N, and Ni in the NiNCB-sim 800 °C catalyst.

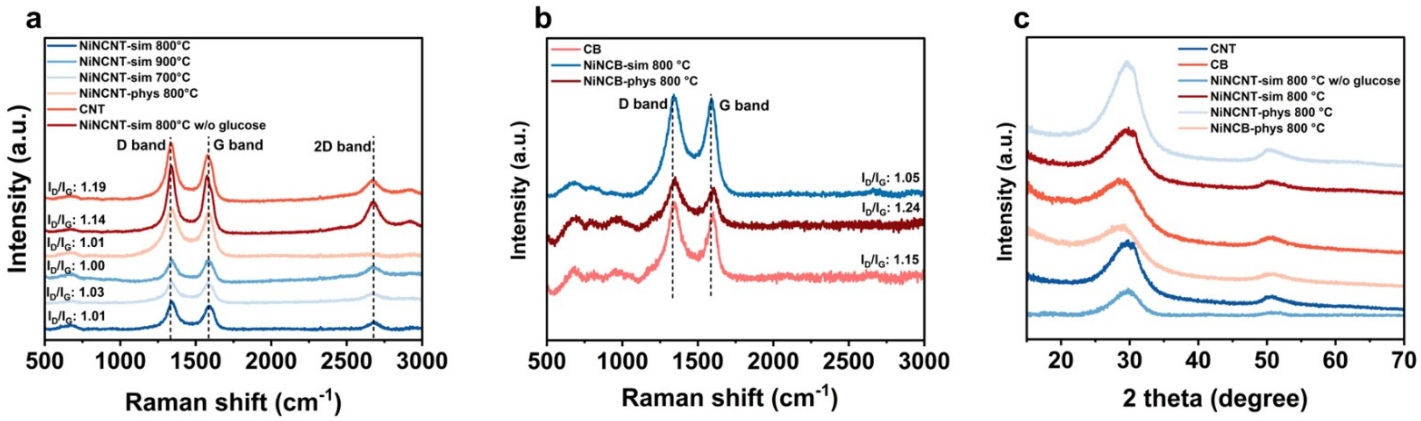

Fig. S8 | a, Raman spectra and I_D/I_G ratio for NiNC catalysts synthesized using CNT substrate, simultaneous melamine impregnation, different pyrolysis temperatures, and glucose effect, **b,** Raman spectra and I_D/I_G ratio for CB, NiNCB-sim 800 °C, NiNCB-phys 800 °C catalysts, **c,** XRD results for CNT, CB, NiNCB-phys 800 °C, NiNCNT-phys 800 °C, NiNCNT-sim 800 °C, and NiNCNT-sim 800 °C w/o glucose catalysts.

Table S3. Elemental composition of NiNC catalysts. N contents determined by XPS and Ni loading contents determined by ICP-MS.

Catalyst	Rel. abundance of N groups (%)					Atomic percentage (%)		Ni content wt.% (ICP-OES)
	pyridinic	pyrrolic	graphitic	oxide	Ni-N	N	Ni	
NiNCNT-sim 700 °C	53.18	18.56	11.11	4.54	12.61	5.55	0.49	0.55
NiNCNT-sim 800 °C	29.75	28.8	11.46	5.03	24.97	1.21	0.53	0.66
NiNCNT-sim 900 °C	33.22	24.1	14.88	2.74	25.06	1.3	0.52	0.72
NiNCNT-phys 800 °C	43.38	17.49	20.54	5.27	13.32	3.67	0.42	0.67
NiNCB-phys 800 °C	56.34	24.83	11.88	3.00	3.95	1.26	0.10	0.68
NiNCNT-sim 800 °C w/o glucose	44.27	25.61	13.85	5.73	10.54	0.96	0.50	0.59

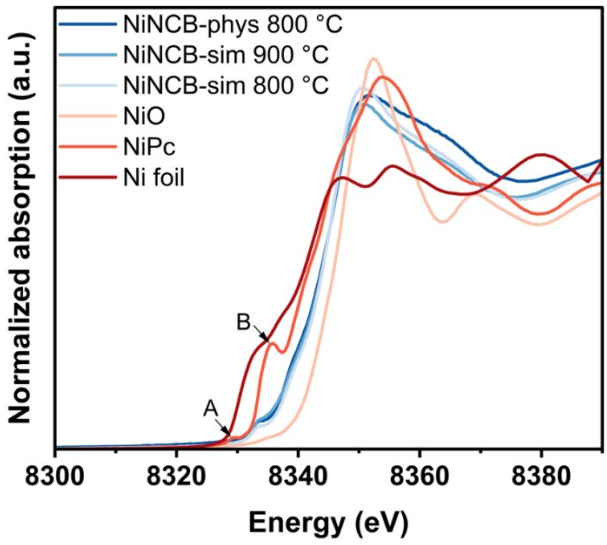

Fig. S9 | Ni K-edge XANES spectra of the NiNCB catalysts and references.

Table S4. EXAFS fitting parameters at the Ni K-edge for NiNCNT-sim 700 °C, NiNCNT-sim 800 °C, NiNCNT-sim 900 °C, and NiNCB-sim 800 °C catalysts（$S0^2$=1).

Catalyst	Bond	CN*	R (Å)	σ^2 (Å^2)	ΔE_0 (eV)	R factor (%)	Reduced chi-square
NiNCNT-sim 700 °C	Ni-N	4.08±0.83	1.92±0.15	0.007±0.0005	5.82±1.43	1.52	92.87
NiNCNT-sim 800 °C	Ni-N	4.12±0.88	1.93±-0.02	0.003±0.0007	8.71±0.67	1.39	79.87
NiNCNT-sim 900 °C	Ni-N	3.32±0.29	1.89±0.06	0.0056±0.0007	1.88±0.21	1.93	63.14
NiNCB-sim 800 °C	Ni-N	4.31±0.32	1.99±0.08	0.0055±0.0001	9.72±1.21	1.06	34.43

* Coordination number

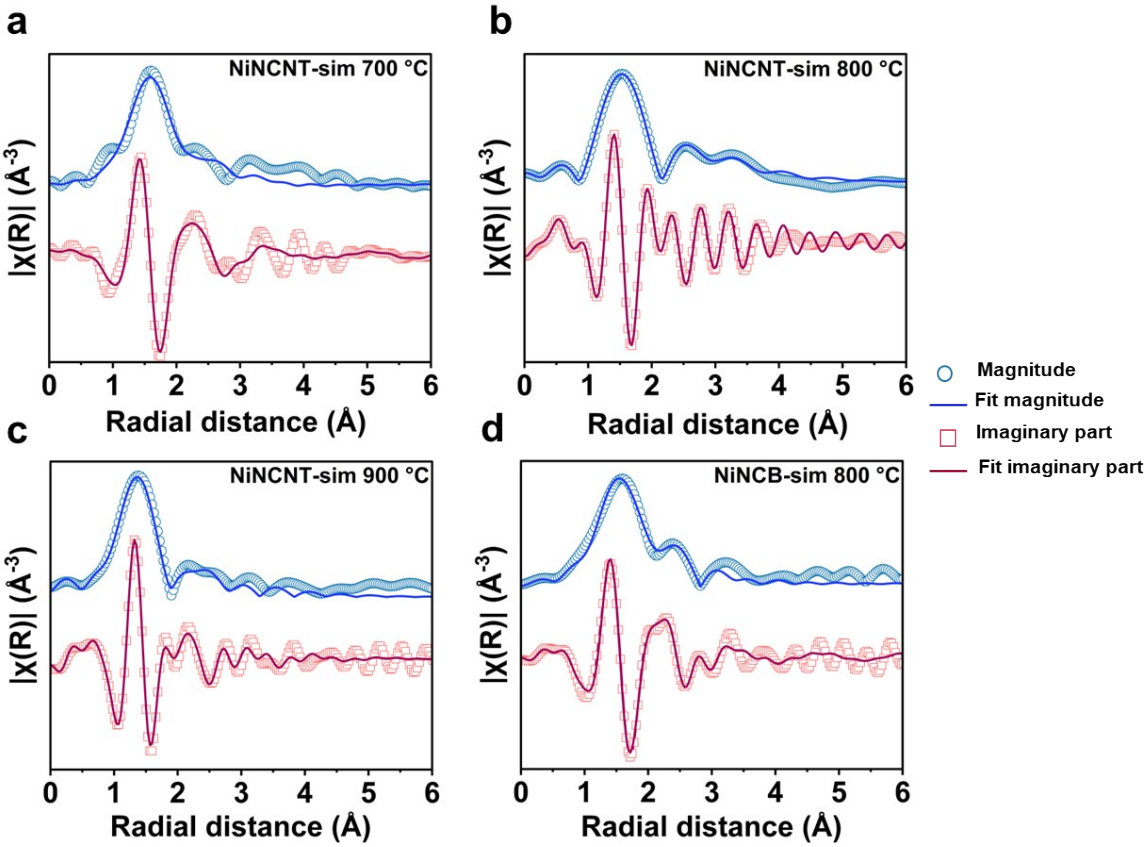

Fig. S10 | Fitting of EXAFS spectra for **a,** NiNCNT-sim 700 °C, **b,** NiNCNT-sim 800 °C, **c,** NiNCNT-sim 900 °C, and **d,** NiNCB-sim 800 °C catalysts.

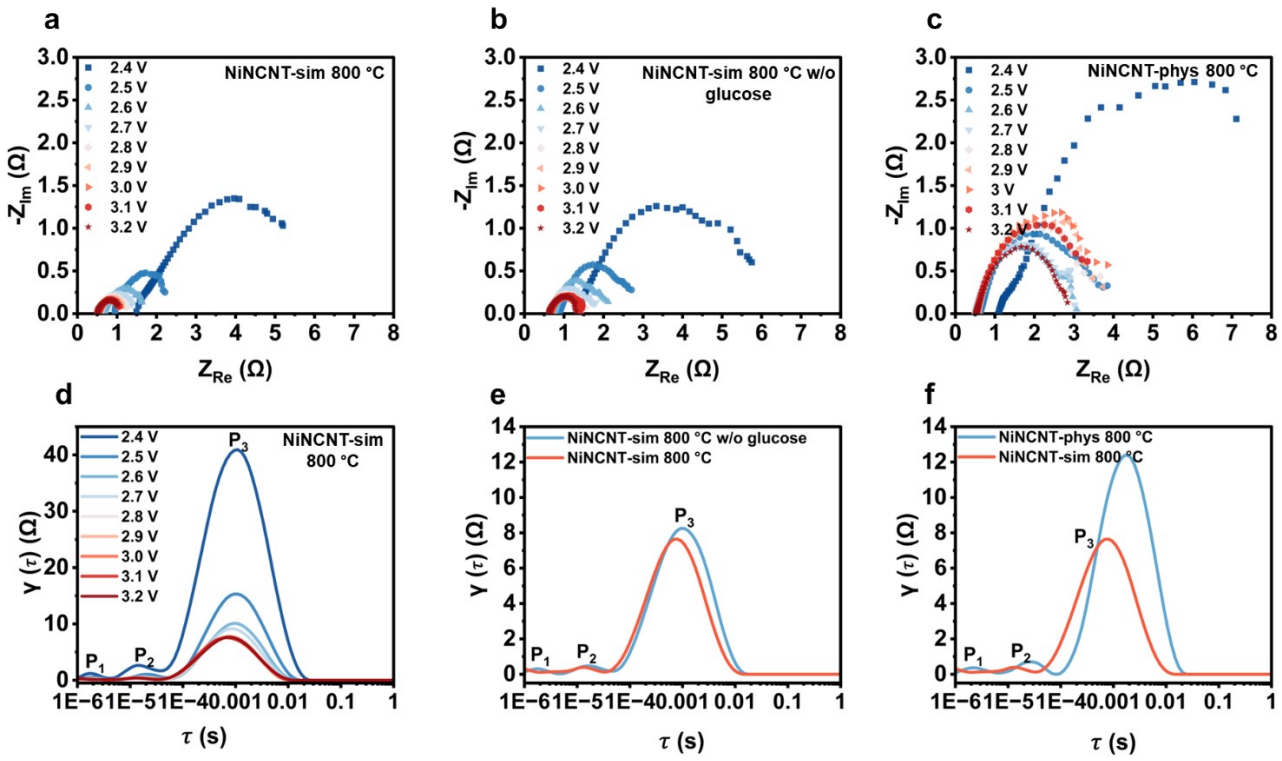

Fig. S11 | **a,** *in situ* EIS results of the NiNCNT-sim 800 °C, **b,** NiNCNT-sim 800 °C w/o glucose, **c,** NiNCNT-phys 800 °C, **d,** DRT diagrams of the NiNCNT-sim 800 °C at different cell voltages, **e,** effect of chelating agent on the DRT graphs of NiNCNT-sim 800 °C catalyst at 3.2 V, and **f,** role of catalyst preparation results on relaxation times at 3.2 V. All tests were performed in a MEA, using 0.5M $KHCO_3$ as anolyte.

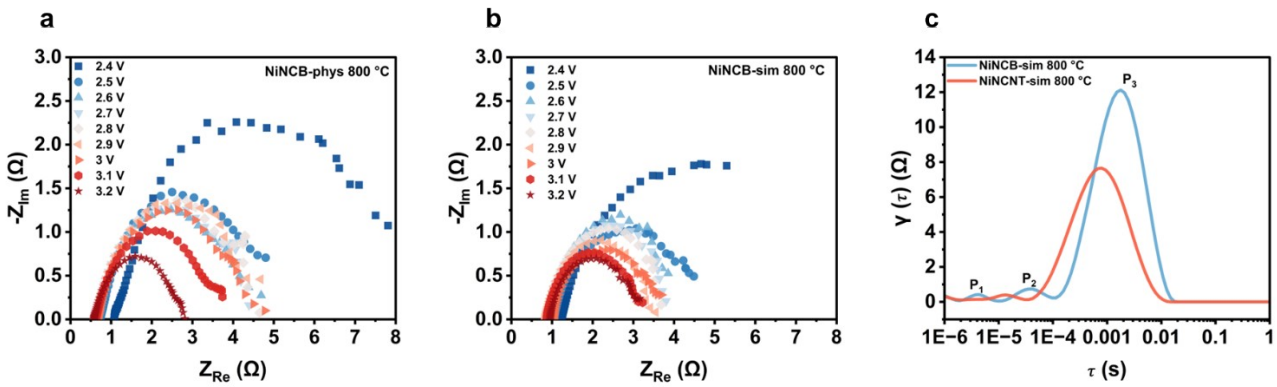

Fig. S12 | a, *in situ* EIS results of the NiNCB-phys 800 °C, **b,** NiNCB-sim 800 °C, and **c,** DRT diagram of the NiNCNT-sim 800 °C and NiNCB-sim 800 °C electrodes at 3.2 V. All tests were performed in a MEA, using 0.5M $KHCO_3$ as anolyte.

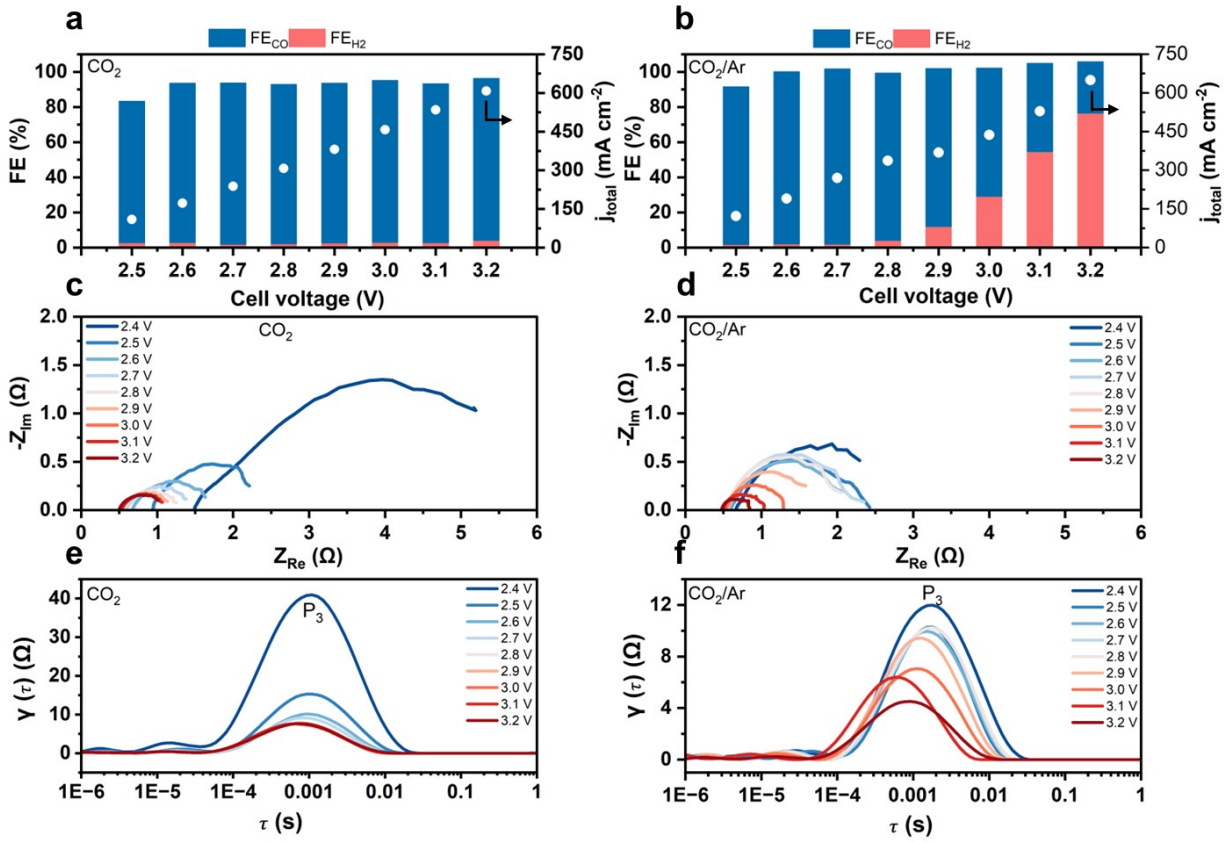

Fig. S13 | CO_2R performance of NiNCNT-sim 800 °C electrode **a,** under CO_2 atmosphere, **b,** CO_2/Ar atmosphere (1:1 ratio), *in situ* EIS results of the NiNCNT-sim 800 °C, **c,** under CO_2 atmosphere, d, CO_2/Ar atmosphere (1:1 ratio), DRT diagram of the NiNCNT-sim 800 °C electrode **e,** under CO_2 atmosphere, **f,** CO_2/Ar atmosphere (1:1 ratio). All tests were performed in a MEA, using 0.5M $KHCO_3$ as anolyte.

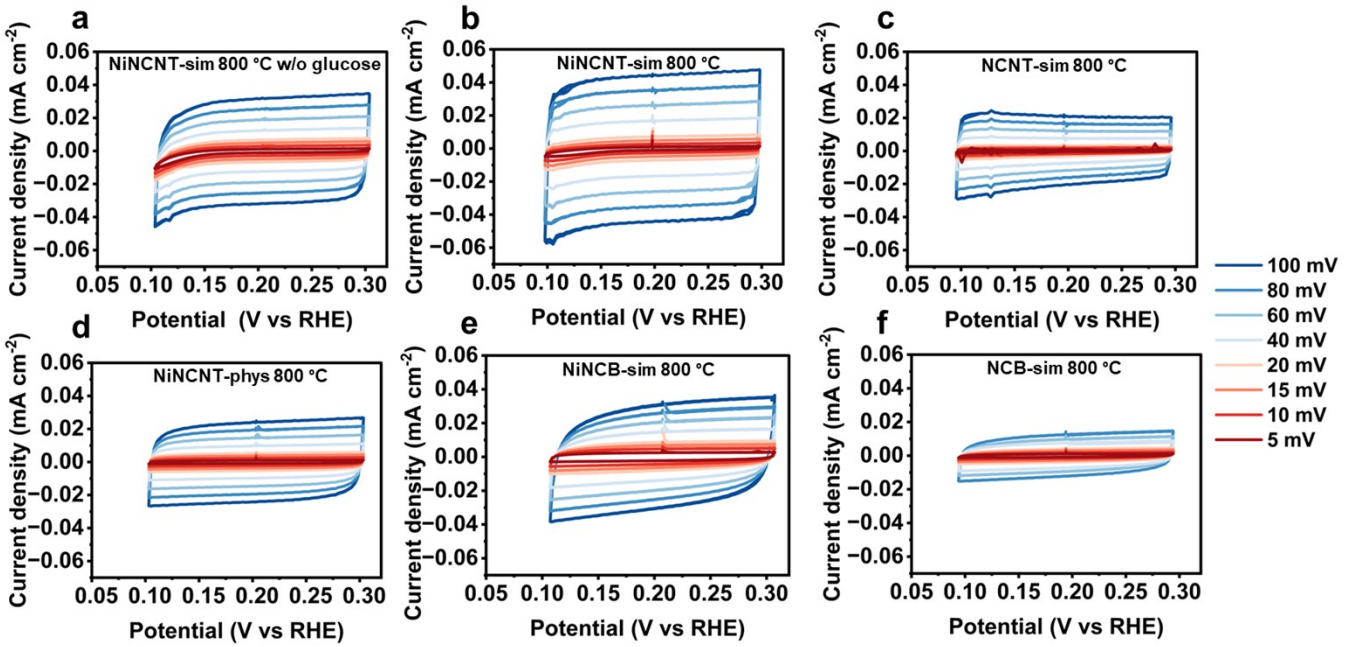

Fig. S14 | Cyclic voltammetry of different samples in 0.5 M $KHCO_3$ at scan rates of 5, 10, 15, 20, 40, 60, 80, and 100 $mV.s^{-1}$: **a,** NiNCNT-sim 800 °C w/o glucose, **b,** NiNCNT-sim 800 °C, **c.** NCNT-sim 800 °C, **d,** NiNCNT-phys 800 °C, **e,** NiNCB-sim 800 °C, and **f,** NCB-sim 800 °C.

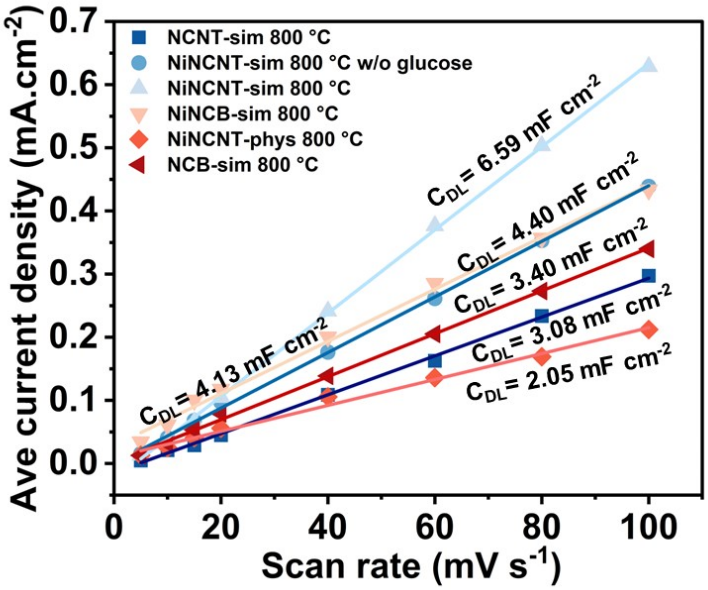

Fig. S15 | Double layer capacitance of the prepared electrodes.

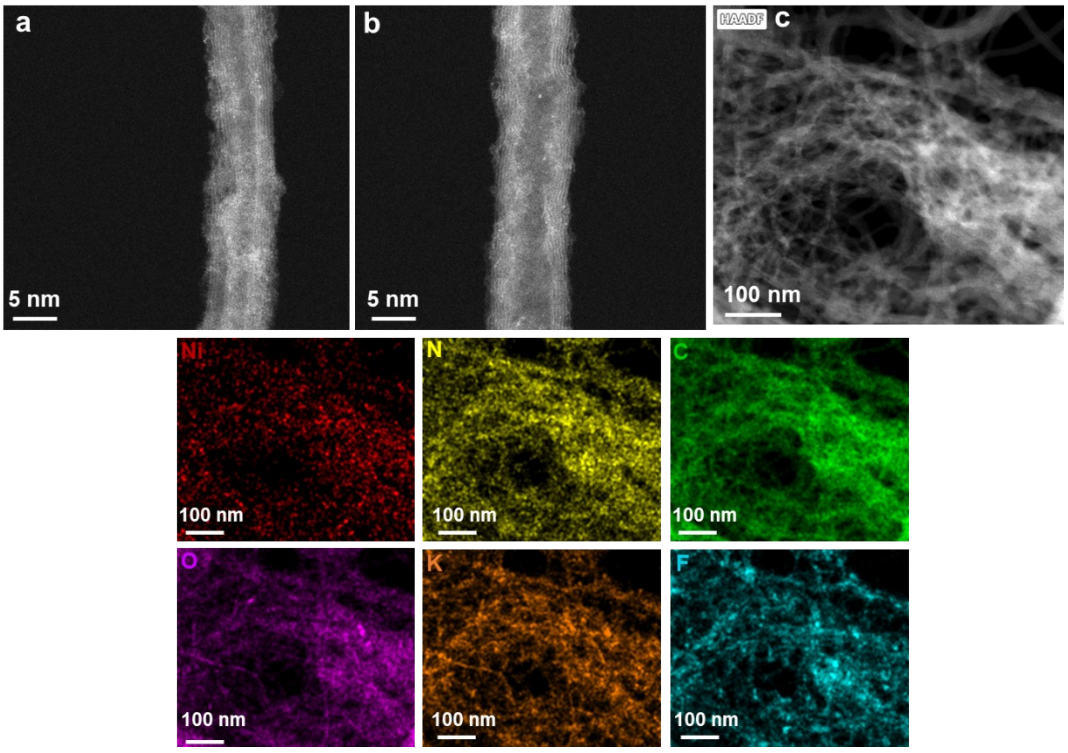

Fig. S16 | a, b, HAADF-STEM images showing atomically dispersed Ni species in NiNCNT-sim 800 °C catalyst after stability testing at 200 mA cm^{-2} using pulse chronopotentiometry (3s at 200 mA cm^{-2}, 1s at 0 mA cm^{-2}) for 70 h, and **c,** Elemental mapping (EDX) of NiNCNT-sim 800 °C catalyst after stability testing at 200 mA cm^{-2}.

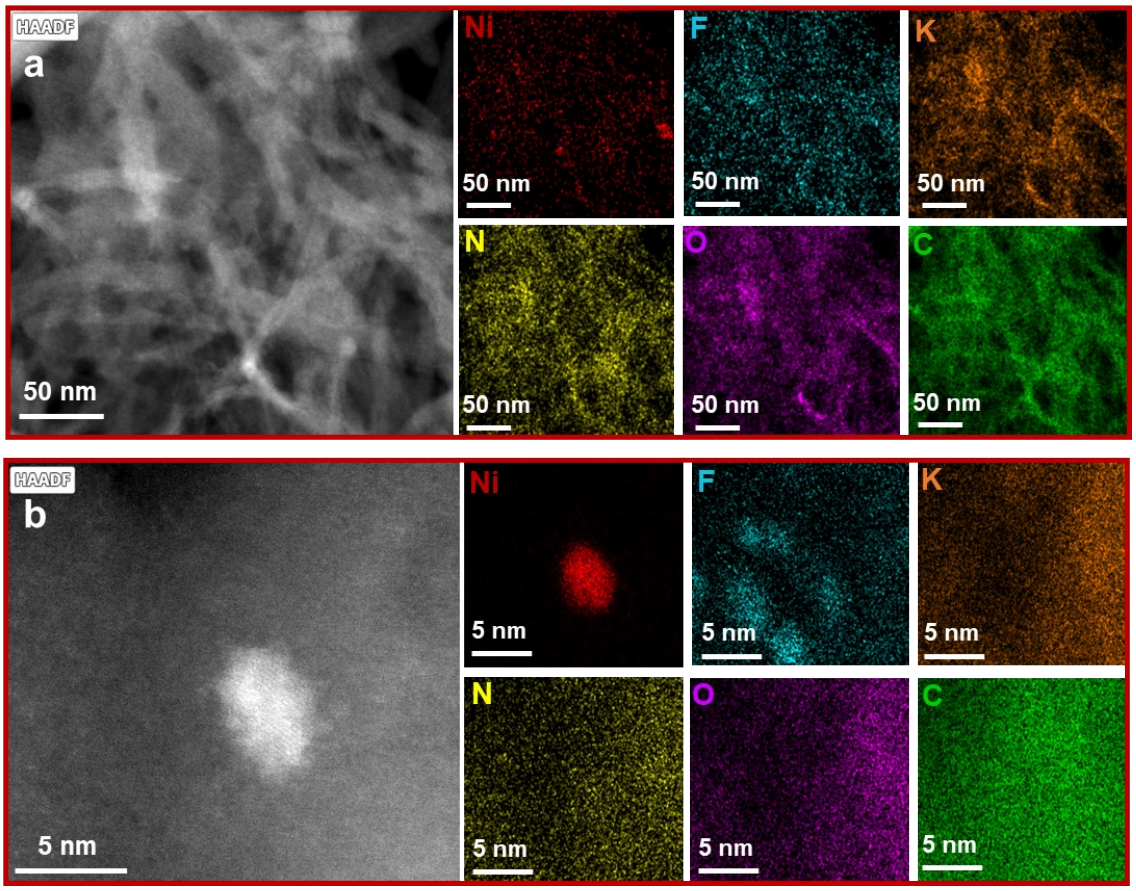

Fig. S17 | a, b, Elemental mapping (EDX) of NiNCNT-sim 800 °C catalyst after stability testing at 200 mA cm^{-2} using pulse chronopotentiometry (3s at 200 mA cm^{-2}, 1s at 0 mA cm^{-2}) for 70 h, indicating formation of Ni nanoparticles.

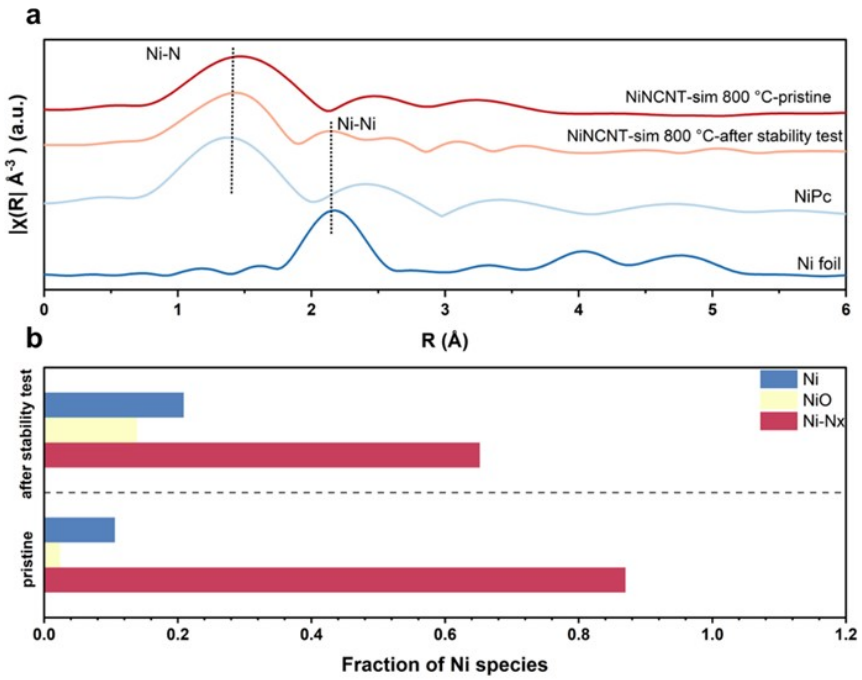

Fig. S18 | a, FT-EXAFS spectra at the Ni K-edge of the NiNCNT-sim 800 °C catalyst after stability test at 200 mA cm^{-2} using pulse chronopotentiometry (3s at 200 mA cm^{-2}, 1s at 0 mA cm^{-2}) for 70 hours, and **b,** Fraction of Ni species in the pristine NiNCNT-sim 800 °C and after stability test at 200 mA cm^{-2} using pulse chronopotentiometry (3s at 200 mA cm^{-2}, 1s at 0 mA cm^{-2}) for 70 hours, derived from linear combination fitting analysis.

Supplementary Note 1.

The FIB-SEM datasets were acquired at voxel sizes of 4 nm for NiNCB-sim 800 °C and 2 nm for NiNCNT-sim 800 °C catalysts, ensuring that nanoscale structural features are captured. To balance geometric fidelity with computational cost, the simulation domain was limited to a three-dimensional sub-volume of 250 × 250 × 250 nm³. This represents the largest domain that can be practically resolved in COMSOL Multiphysics within our current computational capacity while preserving the detailed features of the reconstructed microstructure. Recognizing that a single domain of this size cannot fully capture the inherent heterogeneity of the catalyst layer, three sub-volumes were randomly selected from distinct regions of each sample and simulated independently. This approach enables us to account for heterogeneity of the catalyst layers while remaining within feasible computational limits. Each sub-volume was decomposed into two complementary computational domains: the pore (gas) phase, which governs gas flow (Stokes equations) and gas diffusion (Fick's law), and the solid phase (catalyst structure), which resolves electronic transport via Ohm's law. The solid phase (consisting of carbon and binder) was used for the steady-state electric current simulations, whereas the pore phase (void space) was utilized for fluid flow and CO_2 transport simulations. The resulting transport properties were averaged to capture the representative behavior while accounting for inherent structural heterogeneity. All simulations were carried out in COMSOL Multiphysics using creeping-flow, transport of diluted species, and electric current physics interfaces under steady-state conditions.

Fluid Flow: To evaluate the CO_2 gas permeability within the porous catalyst layers for each sub-volume, steady-state fluid flow through the pore network was simulated by solving the Stokes equations, the momentum balance and continuity equations (**Table S5**). Dirichlet boundary condition of constant pressure was applied in the inlet and outlet boundaries. porous sample. The solid phase was treated as a stationary wall ($u = 0$) to enforce no-slip condition. The volumetric flow rate, $Q\ [m^3.s^{-1}]$, was computed by integrating the normal velocity over the outlet boundary. The permeability, k, of the porous structure was then determined by Darcy's law (**Table S5**). The average permeability for three independent domains for each catalyst layer, are reported in **Table S6**.

Mass Transport: Fick's law under steady-state condition was solved for each sub-volume to find the effective diffusivity, D_{eff}, of CO_2 through the catalyst layers.

Dirichlet boundary condition of constant was applied as the boundary condition between at inlet and outlet boundaries. All other walls and the pore-solid interfaces were treated as no-flux boundaries, impermeable to gas diffusion. Using the total molar flow (integration of the normal diffusive flux over the outlet boundary) and Fick's law, $^{D_{eff}}$ was evaluated. The average effective CO_2 diffusivities for three distinct domains are depicted in **Table S6**.

Electrical Conductivity: The effective electrical conductivity of each catalyst layer was obtained by solving steady-state form of Ohm's law within the 3D solid phase. Dirichlet boundary condition of constant electric potential difference was imposed at the inlet and outlet boundaries. All other walls were defined as the electrically insulating boundary (zero normal current). The effective electrical conductivity, $^{\sigma_{eff}}$, through the catalyst layer was calculated by integrating normalized current density over the outlet surface and applying Ohm's law. The catalyst conductivity for three different domains for each catalyst layer, are summarized in **Table S6**.

Table S5. Governing equations, boundary conditions, and parameters used in the numerical simulations for evaluating transport properties.

	Governing equation	Boundary conditions	Parameters	
Fick's law	$\nabla.(-D\nabla c) = 0$	c_{inlet}: Dirichlet boundary condition, constant concentration c_{outlet}: Dirichlet boundary condition, constant concentration No flux at walls ($n.j = 0$)	D_0: gas diffusion coefficient D: diffusivity c: concentration [mol/m^3] j: molar flux [mol/s]	D_0 = 1.6 E-05 m^2/s
Stokes and continuity equations	$\mu\nabla^2 u - \nabla p = 0$ $\nabla.u = 0$	P_{inlet}: Dirichlet boundary condition, constant pressure P_{outlet}: Dirichlet boundary condition, constant pressure No slip at walls ($u = 0$)	u: gas velocity [m s^{-1}] p: pressure [Pa] μ: gas dynamic viscosity [Pa.s] ρ: density [kg/m^3]	μ = 1.5 E-06 $Pa.s$ ρ = 1 kg/m^3
Darcy's law	$\frac{Q}{A} = \frac{k\nabla p}{\mu L}$	-	Q:$flow\ rate\ [m^3.s^{-1}]$ k: permeability [m^2] A: layer area [m^2] L: layer thickness [m]	A = 250 × 250 nm^2 L = 250 nm
Ohm's law	$\nabla.(-\sigma\nabla\phi) = 0$	ϕ_{inlet}: Dirichlet boundary condition,	σ: electric conductivity ϕ: electric potential [mol/m^3]	$\sigma_{carbon\ black}$ = 550 S/m

	constant electric potential ϕ_{outlet}: Dirichlet boundary condition, constant electric potential Electric insulation at walls ($n.J = 0$)	J: current density [A]	$\sigma_{carbon\ nanotube} =$ 50000 S/m

Table S6. Transport parameters derived from 3D simulations for the NiNCNT and NiNCB catalyst layers. Values are the mean ± standard deviation from three randomly selected sub-volumes (250 × 250 × 250 nm^3) per catalyst layer.

Catalyst	Effective diffusivity, D (m^2 s^{-1})		Permeability, k (m^2)		Effective conductivity, σ (S m^{-1})	
NiNCNT-sim 800 °C	1.03E-05	1.17±0.25E-05 (average)	4.17E-16	3.87±0.49 E-16 (average)	672.56	669.29± 84.38 (average)
	1.47E-05		3.30E-16		583.36	
	1.04E-05		4.13E-16		751.96	
NiNCB-sim 800 °C	6.43E-06	6.51±0.48E-06 (average)	1.42E-16	1.47±0.41E-16 (average)	122.59	148.00±29.54 (average)
	6.07E-06		1.07E-16		180.78	
	7.02E-06		1.90E-16		140.98	

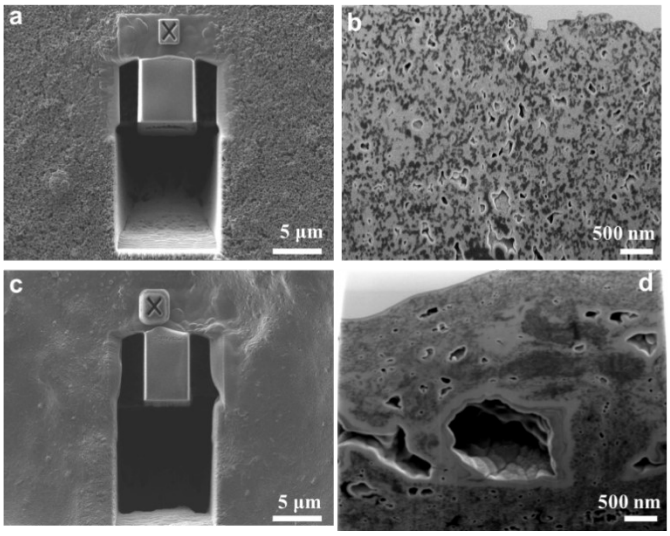

Fig. S19 | Site preparation and FIB cross sections of **a, b,** NiNCB-sim 800 °C, and **c,d,** NiNCNT-sim 800°C catalyst layers.

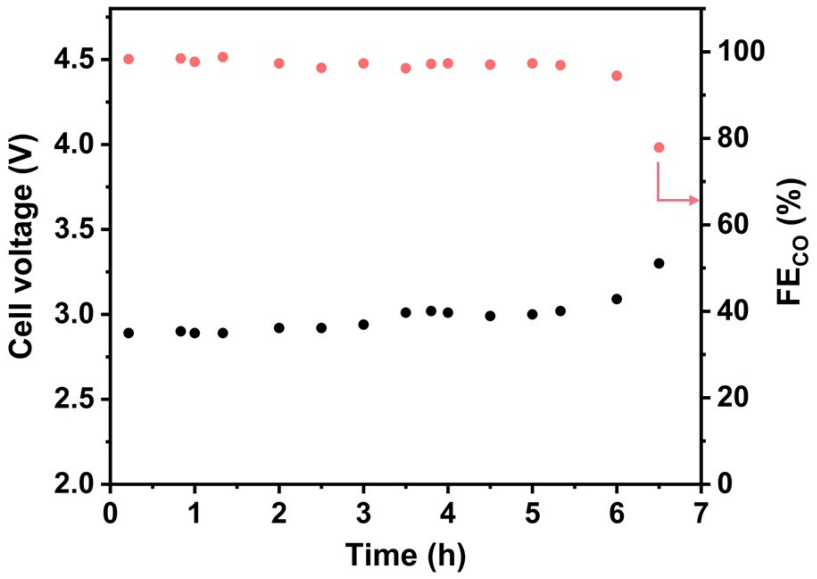

Fig. S20 | Stability of the NiNCB-sim 800 °C in a MEA under pulsed chronopotentiometry (3 s at 200 mA cm^{-2}, 1 s at 0 mA cm^{-2}) using 0.1M $KHCO_3$ electrolyte.

Supplementary Note 2.

Determining an exact value for the limiting current density in porous electrodes, particularly in membrane electrode assembly (MEA) configurations, remains inherently challenging. For non-porous flat electrodes in simplified H-cell systems, the limiting current density can be estimated analytically using a classical Fickian diffusion expression (14)

$$j_{lim} = \frac{nFD_{eff}C_{CO_2}}{L_{eff}}$$

where n is the number of electrons transferred, F is Faraday's constant, C_{CO_2} is the reactant concentration, and L_{eff} is the effective transport length scale (measured using SEM cross section images, **Fig. S21**). While this model is valid for flat, non-porous electrodes, it is used here as a qualitative metric to enable comparison of relative transport characteristics between the NiNCNT-sim 800 °C and NiNCB-sim 800 °C catalyst layers. The effective diffusivity values for both catalyst layers and the corresponding limiting current densities are shown in **Table S7**. These values provide a comparative basis for evaluating the relative transport capabilities of the investigated electrodes and identifying regimes where CO_2 supply may constrain performance. It should be noted that these analytical estimates are inherently qualitative. The equation relies on simplified assumptions, including (i) steady-state Fickian diffusion, (ii) uniform and isotropic pore structure, and (iii) a single-phase transport description with constant properties. In practical CO_2 electrolyzers, however, transport is strongly influenced by multiphase effects, including gas–liquid coexistence, dynamic wetting, and carbonate formation, which alter both the effective diffusivity and the accessible transport pathways (15). In addition, spatial variations in the reaction rate leads to non-uniform reactant depletion across the catalyst layer, such that the effective transport length scale deviates from the physical thickness estimated using cross-section SEM image. As a result, the analytical expression provides only an approximate indication of transport limitations and should be interpreted as a qualitative metric rather than a predictive model.

Unlike non-porous electrodes in H-cell systems, where transport can often be approximated by purely diffusive fluxes, CO_2 transport in porous gas diffusion layers arises from a coupled interplay between diffusion and convection. This coupled transport behavior has been extensively studied in the literature to elucidate its impact on electrochemical performance (16–18).

The diffusive flux of CO_2 is described by Fickian transport and is commonly parameterized using an effective diffusivity (D_{eff}), which accounts for structural characteristics such as porosity, tortuosity, and constrictivity. In parallel, convective transport can contribute significantly under MEA operating conditions and is governed by Darcy's law, where the permeability (K) of the catalyst layer determines the extent of pressure-driven flow through the porous network. Within this study, the high-resolution FIB-SEM tomography (voxel size ~2 nm) combined with direct numerical simulations provides quantitative insights into the structure-transport relationship. The

reconstructed pore networks indicate that the NiNCNT-sim 800 °C catalyst layer exhibits superior transport characteristics compared to the NiNCB-sim 800 °C counterpart. Specifically, the effective diffusivity is approximately 80% higher ($^{D_{eff,CNT}}/_{D_{eff,CB}} \approx 1.8$), while the permeability is enhanced by a factor of ~2.6 ($^{K_{CNT}}/_{K_{CB}} \approx 2.6$). These results indicate that CNT-based catalyst layer facilitate both diffusive transport and convective penetration of CO_2 into the porous structure. This concurrent enhancement of diffusive and convective transport is directly reflected in the CO_2R performance. In the CB-based system, the partial density towards CO reaches a plateau at approximately 200 mA cm^{-2}, beyond which no further increase is observed. This behavior can be correlated with mass transport limitations, where insufficient CO_2 delivery to active sites constrains the reaction rate. On the other hand, the CNT-based electrode (NiNCNT-sim 800 °C) does not exhibit a comparable limitation within the investigated range, achieving partial current density towards CO as high as ~550 mA cm^{-2} (**Fig. S22**). This suggests that improved pore connectivity and transport pathways in the NiNCNT-sim 800 °C catalyst layer can contribute to mitigate CO_2 depletion within the catalyst layer. Overall, these results demonstrate that CO_2R performance in MEA electrolyzers is governed not only by intrinsic catalytic activity but also, critically, by the coupled diffusive and convective transport properties dictated by the electrode microstructure.

Table S7. Limiting current density for NiNCNT-sim 800 °C and NiNCB-sim 800 °C electrodes using Fickian diffusion expression.

Catalyst	D_{eff} (m^2 s^{-1})	(P) (atm)	(T) (K)	C_{CO2} (mol m^{-3})[a]	L_{eff} (μm)[b]	$j_{lim, CO}$ (mA cm^{-2})[c]
NiNCNT-sim 800 °C	1.17E-05	1.1	298	44.98	70	145.09
NiNCB-sim 800 °C	6.51E-06	1.1	298	44.98	80	70.64

a: $C_{CO_2} = \frac{P}{RT}$

b: derived from SEM cross-section image (average thickness)

c: $j_{lim} = \frac{nFD_{eff}C_{CO_2}}{L_{eff}}$

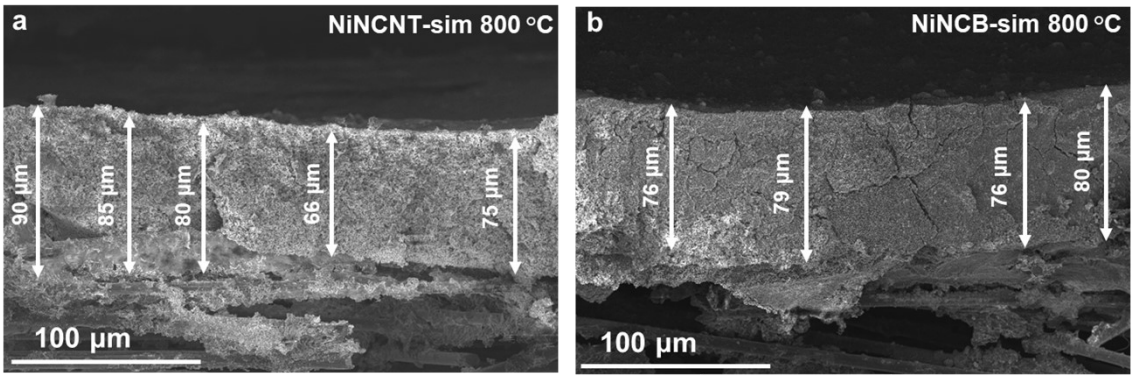

Fig. S21 | SEM cross-section images of **a,** NiNCNT-sim 800 °C and **b,** NiNCB-sim 800 °C electrodes.

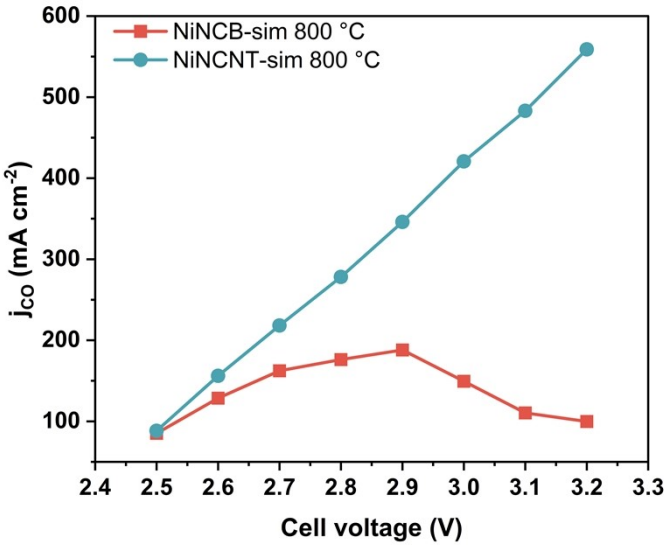

Fig. S22 | Partial current density towards CO (j_{CO}) for NiNCB-sim 800 °C and NiNCNT-sim 800 °C electrodes using 0.5M $KHCO_3$ electrolyte in MEA.

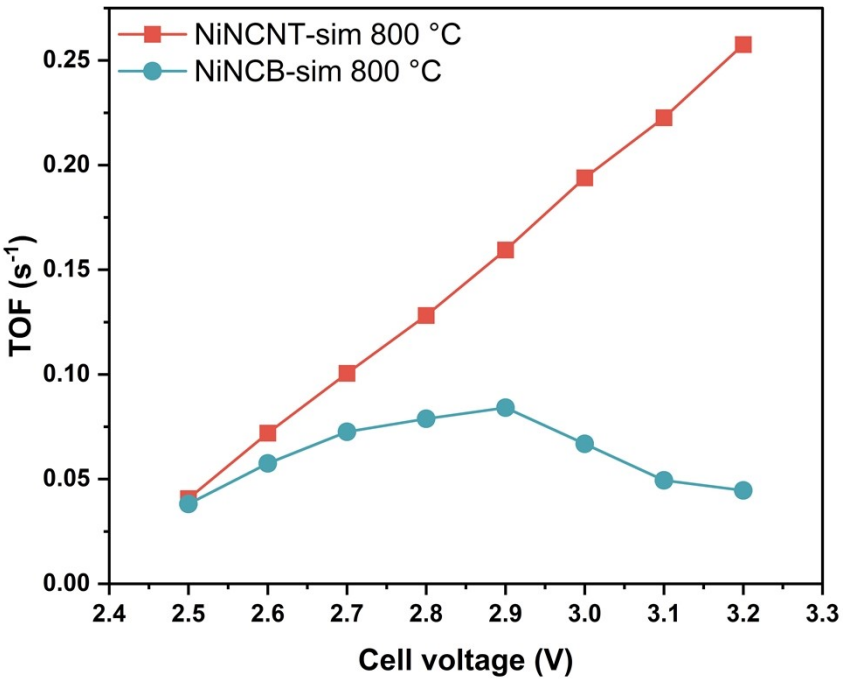

Fig. S23 | Turnover frequency (TOF) of NiNCB-sim 800 °C and NiNCNT-sim 800 °C catalysts as a function of applied cell voltage in the MEA.

Supplementary Note 3.

We used the two methods provided by CatCost to estimate the processing costs associated with the best performing catalyst (NiNCNT-sim 800 °C) developed in this paper (19,20). In the step method (catalysts synthesised by a contract manufacturer), flat hourly rates are used for specific pieces of the equipment and is accurate to within 20% of the market prices for various catalyst materials. The second method (suitable for large quantity productions) involves a detailed assessment of the capital costs (CapEx) and operating costs (OpEx) based on the established best practises in process engineering. By estimating the major components of a process plant and applying factors or multipliers to estimate the cost of secondary components, this approach provides a reasonably accurate preliminary cost estimate. To this end, CatCost equipment library, which includes cost information for over 200 pieces of chemical processing equipment, installation cost variables, and direct labour requirements was employed. Cost multipliers are used to account for the various construction materials. Operating costs are estimated considering the direct labour requirements and other cost components such as equipment investment. In this study we implemented two methods for estimating NiNCNT-sim 800 °C synthesis cost: step method (which is mainly for production scales smaller than a few kilotons per year), and CapEx/OpEx factors

method (larger volumes). In the first approach, individual synthesis steps, each corresponding to a specific equipment typically used by a contract catalyst manufacturer, are selected from an established database to build a bottom-up cost estimate. On the other hand, in the second method, the primary component of the capital cost for catalyst synthesis is derived from cumulative purchase cost of the required process equipment (e.g., reactor vessels, filters). The cost of equipment is estimated using the established cost correlations published in the chemical engineering design literature. The synthesis method for atomically dispersed NiNCNT-sim 800 °C catalyst in this study closely parallels the synthesis method for thermocatalysts, such as Fluid Catalytic Cracking (FCC) catalyst. Accordingly, similar industrial-scale equipment was selected to model a scalable process based on the lab-scale protocol, with efficiency adjustments. The process templates included in CatCost (e.g., fluid catalytic cracking) were consulted as a guide to establish the commercial scale synthesis process for NiNCNT catalyst (**Fig. S24**). The value of spent catalyst at the end of its useful life plays a key role in estimating the total cost. CatCost accounts for the value of spent catalysts by considering three possible outcomes: metal recovery, sale for alternative uses, or disposal at cost. The software calculates the recoverable metal content (in this case Ni); its value and the costs associated with metal recovery. The spent catalyst value (SCV) can offset the estimated cost of purchasing the catalyst if it exceeds other disposal options. The SCV is reported separately to facilitate decision making analysis. The inputs and outputs of the CatCost for both methods are depicted in **Fig. S25-27**. All prices were adjusted to 2022 US$ using the US Bureau of Labor Statistics Chemical Producer Price Index or, for equipment costs, the Chemical Engineering Plant Cost Index (CEPCI).

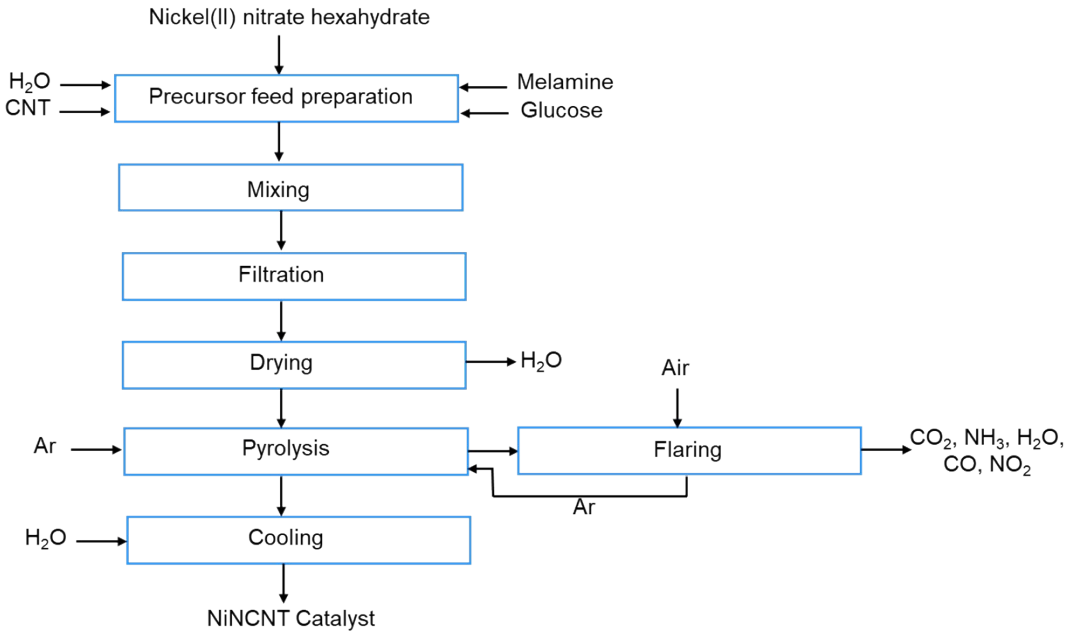

Fig. S24 | Proposed synthesis process for preparing atomically dispersed NiNCNT catalyst. Used as the basis for cost estimation.

CatCost v1.1.0 Summary – 1 Inputs
Estimate: NiNC

Global Inputs

Economics	
Basis Year	2021
Currency	USD ($)
Output Units	
Mass Unit	kg

Processing Cost Estimation Inputs – Step Method

Synthesis Campaign Size	ValueUnits
Order size (1-1000 tons)	2ton
Equipment size	Small (1 ton/day)
Synthesis time	2days
Cleaning time	0.5days
Total Synthesis campaign length	2.5days
Overhead and Selling Margin	
G&A Overhead	5%
R&D Overhead	5%
Selling Margin	33.00%

Processing Cost Estimation Inputs – CapEx & OpEx Factors

Production Capacity - Catalyst	ValueUnits
Design Production, Annual	2.00E+04kg
Capacity Factor	100%
Actual Production, Annual	2.00E+04kg
Production Capacity - Operating Hours	
Operating Hours (Labor)	8760hours
On-Stream Factor	90%
Operating Hours (Production)	7884hours
Design Production Rate	2.54E+00kg/hr
Plant Life	
Plant Life (for depreciation)	10years
Selling Margin	
Calculate using (select):	ROI
Return on capital invested (pre-tax)	25%/year
Flat margin (% of costs)	%

CatCost v1.1.0 Summary – 3a Step Method
Estimate: NiNC

Step Method: Inputs and Total Processing Costs

From CatCost "1 Inputs" Sheet	
Order size in tons	2ton
Order size in model units	1,814kg
Equipment size	Small (1 ton/day)
Synthesis campaign length	2.50days
Process Template Selected	Custom Step Process

Step Method Costs for Selected Process Template

		Cost ($/kg catalyst)	Cost ($/year)
Cost ($/hr)	$547	213.0630	4,261,260
Cost ($/campaign)	$32,800		
Cost ($/kg catalyst)	$18.08		

*Outputs consider losses to catalyst

User Entry: Custom Step Process

Step Name	Quantity	Cost ($/hr)	Cost ($/campaign)	Cost ($/kg catalyst)
Incipient wetness (impregnation)	1	82	4,920	2.71
Dryer, rotary (40–100 C)	1	82	4,920	2.71
Filter, belt vacuum	1	137	8,200	4.52
Kiln, batch (300–1290 C)	1	82	4,920	2.71
Reactor, multistep	1	109	6,560	3.62
Flare	1	55	3,280	1.81

Fig. S25 | Screenshots from CatCost estimatations for NiNCNT catalyst. Summary views of CatCost input and output generated using the CatCost 5c Printable Outputs module for Step Method.

CatCost v1.1.0 Summary – 3b Equipment, part 1: inputs
Estimate: NiNC

Process Template or User-Entered Custom Process

Selected Process Template:	Custom Process

Scaling Inputs

Scaling Input Specific to this Process Design/Template		
THIS PROCESS Design Production Rate	2.00E+04	kg catalyst/year
THIS PROCESS Design Production Rate, in Estimate Units	2.54E+00	catalyst/hour
From CatCost "1 Inputs" Sheet (Specific to this Estimate)		
ESTIMATE Design Production Rate	2.54E+00	catalyst/hour

Equipment List: Inputs at This Process Design Production Rate

Equipment Type	User Label	Material of Construction	Quantity	Size	Size Unit
Reactor, jacketed, agitated	1	Carbon steel	1	1	volume, m3
Dryer, indirect-heat steam-tube rotary (Seider)	2	Stainless steel	1	100	Heat-transfer area, ft2
Filter, rotary-drum vacuum	3	Carbon steel and Polypropylene wetted parts	1	10	Filtering area, ft2
Furnace, cylindrical	4	Carbon steel	1	0.2	duty, MW
Flare, ground mounted	5	Standard	1	2500	Waste gas flow rate, lb/hr

CatCost v1.1.0 Summary – 3b Equipment, part 2: outputs
Estimate: NiNC

Equipment Cost Totals

Purchase Cost	**$452,108**
Installed Cost	**$735,336**
Labor Factor (# of operators)	**1.4**

Equipment List: Scaling to Estimate Design Production Rate			*Equipment List: Outputs at Estimate Design Production Rate*		
Equipment Type	Quantity	Size	Purchase Cost	Installed Cost	Labor Factor
Reactor, jacketed, agitated	1	1.0	83,651	142,207	0.3
Dryer, indirect-heat steam-tube rotary (Seider)	1	100.0	65,795	107,904	0.5
Filter, rotary-drum vacuum	1	10.0	156,049	263,723	0.2
Furnace, cylindrical	1	0.2	127,347	193,567	0.3
Flare, ground mounted	1	2,500.0	19,266	27,935	0.1

CatCost v1.1.0 Summary – 3d CapEx
Estimate: NiNC

CapEx & OpEx Factors: Factored Capital Expenditures

Cost Item	Value	Units	Total Cost ($)
Direct Capital			
Purchased Equipment	100	% of purchased equipment cost	452,108
Installation	67	% of purchased equipment cost	302,912
Instrumentation and Controls	26	% of purchased equipment cost	117,548
Piping	31	% of purchased equipment cost	140,153
Electrical	10	% of purchased equipment cost	45,211
Buildings	29	% of purchased equipment cost	131,111
Yard Improvements	12	% of purchased equipment cost	54,253
Service Facilities	55	% of purchased equipment cost	248,659
Waste Treatment	5	% of purchased equipment cost	22,605
Land	6	% of purchased equipment cost	27,126
Total Direct	**341**	**% of purchased equipment cost**	**1,541,688**
Indirect Capital			
Engineering and Supervision	32	% of purchased equipment cost	144,675
Construction Expenses	34	% of purchased equipment cost	153,717
Legal Expenses	4	% of purchased equipment cost	18,084
Contractor's Fee	19	% of purchased equipment cost	85,901
Contingency	37	% of purchased equipment cost	167,280
Total Indirect	**126**	**% of purchased equipment cost**	**569,656**
Total Fixed Capital Investment (FCI)	**467**	**% of purchased equipment cost**	**2,111,344**
Working Capital	75	% of purchased equipment cost	339,081
Total Capital Investment (TCI)	**542**	**% of purchased equipment cost**	**2,450,425**

CatCost v1.1.0 Summary – 3e OpEx
Estimate: NiNC

CapEx & OpEx Factors: Factored Operating Expenditures

Cost Item	Value	Units	Cost ($/year)	Cost ($/kg catalyst)
Direct Labor				
Direct Labor Operators (rounded up)		operators		
Direct Labor Hours per Year		hr/yr		
Direct Labor Rate	48	$/hr		
Direct Labor Cost (DL)			2,102,400	105.1200
Direct Operating Costs				
Supervisory and Clerical Labor	18	% of DL	378,432	18.9216
Laboratory Charges	15	% of DL	315,360	15.7680
Maintenance and Repair (M&R)	5	% of FCI	105,567	5.2784
Operating Supplies	15	% of M&R	15,835	0.7918
Total: Labor, Supplies, Maintenance, Lab (LSM)			**2,917,594**	**145.8797**
Fixed/Indirect Operating Costs				
Local Taxes	2.5	% of FCI	52,784	2.6392
Insurance	0.8	% of FCI	16,891	0.8445
Rent, % of value of rented land	10	% of land	2,713	0.1356
Plant Overhead, % of LSM	60	% of LSM	1,750,557	87.5278
Total: Taxes, Insurance, Rent, Overhead			**1,822,944**	**91.1472**
General Expenses				
Administration	20	% of LSM	583,519	29.1759
Distribution and Marketing	10	% of op. costs excluding PGM/noble metals content	900,219	45.0110
Research and Development	5	% of op. costs excluding PGM/noble metals content	450,110	22.5055
Total: Admin, Dist., Mkting., R&D			**1,933,848**	**96.6924**

CatCost v1.1.0 Summary – 3c Utilities
Estimate: NiNC

Selected Process Template

Selected Process Template:	Custom Process

Process Utilities Consumption and Cost for Selected Template

Utility	Consumption	Units	Unit Cost	Units	Cost ($/kg catalyst)	Cost ($/year)
Cooling Water	0.01	kgal	0.14	$/kgal	0.0014	28
Process Water	0.01	kgal	1.3	$/kgal	0.0130	260
Steam, 150 psig	0.00004	ton	5	$/ton	0.0002	4
Steam, 600 psig	0	ton	5.7	$/ton	-	-
Electricity	0.04	kWh	0.055	$/kWh	0.0022	44
Natural Gas	0.001	MMBtu	3	$/MMBtu	0.0030	60

Utilities Cost Totals

Cost ($/kg catalyst)	Cost ($/year)
0.0198	**396**

Fig. S26 | Summary views of CatCost input and output generated using the CatCost 5c Printable Outputs module for equipment, utilities costs, CapEx, and OpEx.

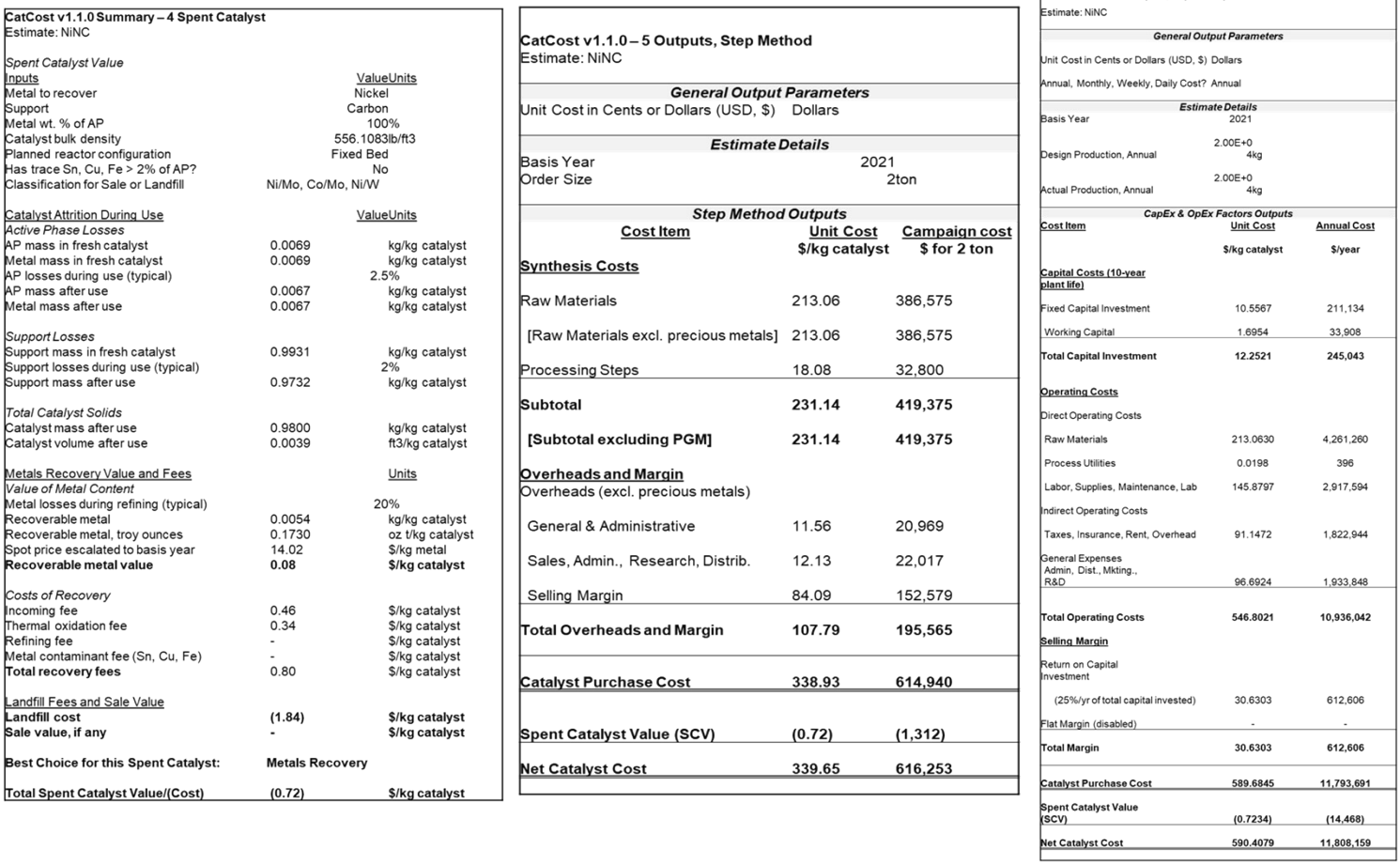

CatCost v1.1.0 Summary – 4 Spent Catalyst
Estimate: NiNC

Spent Catalyst Value

Inputs		ValueUnits
Metal to recover		Nickel
Support		Carbon
Metal wt. % of AP		100%
Catalyst bulk density		556.1083lb/ft3
Planned reactor configuration		Fixed Bed
Has trace Sn, Cu, Fe > 2% of AP?		No
Classification for Sale or Landfill	Ni/Mo, Co/Mo, Ni/W	
Catalyst Attrition During Use		ValueUnits
Active Phase Losses		
AP mass in fresh catalyst	0.0069	kg/kg catalyst
Metal mass in fresh catalyst	0.0069	kg/kg catalyst
AP losses during use (typical)		2.5%
AP mass after use	0.0067	kg/kg catalyst
Metal mass after use	0.0067	kg/kg catalyst
Support Losses		
Support mass in fresh catalyst	0.9931	kg/kg catalyst
Support losses during use (typical)		2%
Support mass after use	0.9732	kg/kg catalyst
Total Catalyst Solids		
Catalyst mass after use	0.9800	kg/kg catalyst
Catalyst volume after use	0.0039	ft3/kg catalyst
Metals Recovery Value and Fees		Units
Value of Metal Content		
Metal losses during refining (typical)		20%
Recoverable metal	0.0054	kg/kg catalyst
Recoverable metal, troy ounces	0.1730	oz t/kg catalyst
Spot price escalated to basis year	14.02	$/kg metal
Recoverable metal value	**0.08**	**$/kg catalyst**
Costs of Recovery		
Incoming fee	0.46	$/kg catalyst
Thermal oxidation fee	0.34	$/kg catalyst
Refining fee	-	$/kg catalyst
Metal contaminant fee (Sn, Cu, Fe)	-	$/kg catalyst
Total recovery fees	0.80	$/kg catalyst
Landfill Fees and Sale Value		
Landfill cost	**(1.84)**	**$/kg catalyst**
Sale value, if any	**-**	**$/kg catalyst**
Best Choice for this Spent Catalyst:	**Metals Recovery**	
Total Spent Catalyst Value/(Cost)	**(0.72)**	**$/kg catalyst**

CatCost v1.1.0 – 5 Outputs, Step Method
Estimate: NiNC

General Output Parameters

Unit Cost in Cents or Dollars (USD, $)	Dollars

Estimate Details

Basis Year	2021
Order Size	2ton

Step Method Outputs

Cost Item	Unit Cost $/kg catalyst	Campaign cost $ for 2 ton
Synthesis Costs		
Raw Materials	213.06	386,575
[Raw Materials excl. precious metals]	213.06	386,575
Processing Steps	18.08	32,800
Subtotal	**231.14**	**419,375**
[Subtotal excluding PGM]	**231.14**	**419,375**
Overheads and Margin		
Overheads (excl. precious metals)		
General & Administrative	11.56	20,969
Sales, Admin., Research, Distrib.	12.13	22,017
Selling Margin	84.09	152,579
Total Overheads and Margin	**107.79**	**195,565**
Catalyst Purchase Cost	**338.93**	**614,940**
Spent Catalyst Value (SCV)	**(0.72)**	**(1,312)**
Net Catalyst Cost	**339.65**	**616,253**

CatCost v1.1.0 – 5 Outputs, CapEx & OpEx Factors
Estimate: NiNC

General Output Parameters

Unit Cost in Cents or Dollars (USD, $)	Dollars
Annual, Monthly, Weekly, Daily Cost?	Annual

Estimate Details

Basis Year	2021
Design Production, Annual	2.00E+0 4kg
Actual Production, Annual	2.00E+0 4kg

CapEx & OpEx Factors Outputs

Cost Item	Unit Cost $/kg catalyst	Annual Cost $/year
Capital Costs (10-year plant life)		
Fixed Capital Investment	10.5567	211,134
Working Capital	1.6954	33,908
Total Capital Investment	**12.2521**	**245,043**
Operating Costs		
Direct Operating Costs		
Raw Materials	213.0630	4,261,260
Process Utilities	0.0198	396
Labor, Supplies, Maintenance, Lab	145.8797	2,917,594
Indirect Operating Costs		
Taxes, Insurance, Rent, Overhead	91.1472	1,822,944
General Expenses Admin, Dist., Mkting., R&D	96.6924	1,933,848
Total Operating Costs	**546.8021**	**10,936,042**
Selling Margin		
Return on Capital Investment		
(25%/yr of total capital invested)	30.6303	612,606
Flat Margin (disabled)	-	-
Total Margin	**30.6303**	**612,606**
Catalyst Purchase Cost	**589.6845**	**11,793,691**
Spent Catalyst Value (SCV)	**(0.7234)**	**(14,468)**
Net Catalyst Cost	**590.4079**	**11,808,159**

Fig. S27 | Summary views of CatCost input and output generated using the CatCost 5c Printable Outputs module for spent catalyst value, Step Method outputs, CapEx and OpEx Factors outputs.

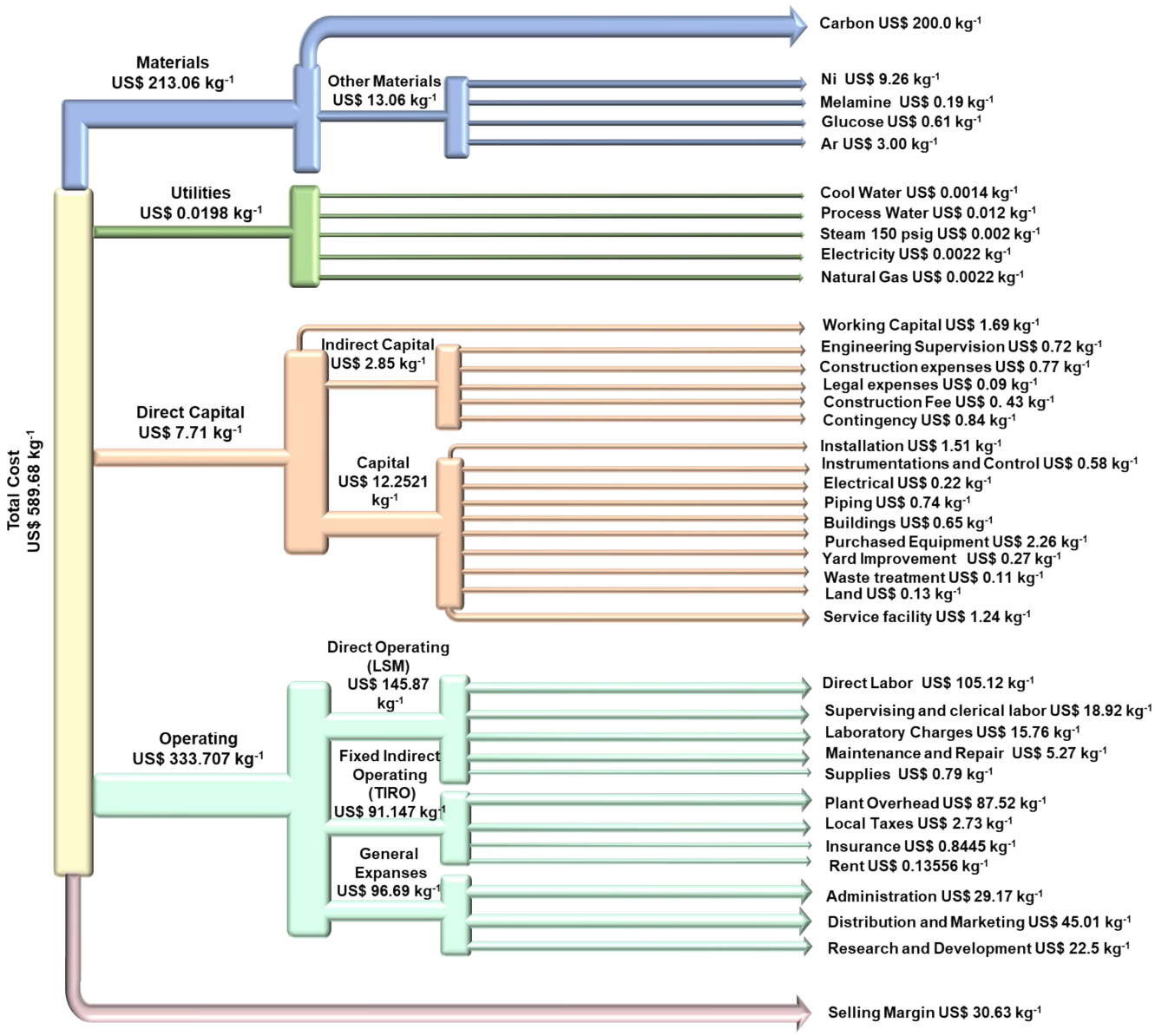

Fig. S28 | Sankey diagram for catalyst cost. Breakdown of contributors to purchase cost for NiNCNT-sim 800 °C catalyst. Line width is proportional to cost contribution. LSM: Laboratory supplies and maintenance; TIRO: Taxes insurance rent and overhead.

References

1. Kim YE, Ko YN, An BS, Hong J, Jeon YE, Kim HJ, Lee S, Lee J, Lee W. Atomically Dispersed Nickel Coordinated with Nitrogen on Carbon Nanotubes to Boost Electrochemical CO_2 Reduction. ACS Energy Lett. 2023 [cited 2025 Jul 31];8(8):3288–96. Available from: https://pubs.acs.org/doi/10.1021/acsenergylett.3c00933

2. Ma Z, Wang B, Yang X, Ma C, Wang W, Chen C, et al. P-Block Aluminum Single-Atom Catalyst for Electrocatalytic CO_2 Reduction with High Intrinsic Activity. J Am Chem Soc [Internet]. 2024 [cited 2025 Jul 31];146(42):29140–9. Available from: https://pubs.acs.org/doi/10.1021/jacs.4c11326

3. Zheng T, Jiang K, Ta N, Hu Y, Zeng J, Liu J, Wang H. Large-scale and highly selective CO2 electrocatalytic reduction on nickel single-atom catalyst. Joule [Internet]. 2019 [cited 2025 Jul 31];3(1):265–78. Available from: https://www.cell.com/joule/fulltext/S2542-4351(18)30506-3

4. Fu S, Izelaar B, Li M, An Q, Li M, de Jong W, Kortlever R. The effect of carbon supports on the electrocatalytic performance of Ni-NC catalysts for CO2 reduction to CO. Nano Energy [Internet]. 2025 [cited 2025 Jul 31];133:110461. Available from: https://www.sciencedirect.com/science/article/pii/S2211285524012138

5. Wang S, Qian Z, Huang Q, Tan Y, Lv F, Zeng L, Shang C, Wang K, Wang G, Mao Y, Wang Y. Industrial-Level CO_2 Electroreduction Using Solid-Electrolyte Devices Enabled by High-Loading Nickel Atomic Site Catalysts. Adv. Energy Mater [Internet]. 2022 [cited 2025 Jul 31];12(31):2201278. Available from: https://onlinelibrary.wiley.com/doi/10.1002/aenm.202201278

6. Leverett J, Yuwono JA, Kumar P, Tran-Phu T, Qu J, Cairney J, et al. Impurity Tolerance of Unsaturated Ni-N-C Active Sites for Practical Electrochemical CO_2 Reduction. ACS Energy Lett. 2022 Mar 11;7(3):920–8. doi:10.1021/acsenergylett.1c02711

7. Hua W, Sun H, Lin L, Mu Q, Yang B, Su Y, et al. A hierarchical Single-Atom Ni-N3-C catalyst for electrochemical CO2 reduction to CO with Near-Unity faradaic efficiency in a broad potential range. Chem. Eng. J [Internet]. 2022 [cited 2025 Jul 31];446:137296. Available from: https://www.sciencedirect.com/science/article/pii/S1385894722027851

8. Zhang M, Wang X, Ding J, Ban C, Feng Y, Xu C, Zhou X. Realizing ampere-level CO2 electrolysis at low voltage over a woven network of few-atom-layer ultralong silverene nanobelts with ultrahigh aspect ratio by pairing with formaldehyde oxidation. Nanoscale [Internet]. 2024 [cited 2025 Nov 3];16(14):7076–84. Available from: https://pubs.rsc.org/en/content/articlelanding/2024/nr/d4nr00361f

9. Endrődi B, Samu A, Kecsenovity E, Halmágyi T, Sebők D, Janáky C. Operando cathode activation with alkali metal cations for high current density operation of water-fed zero-gap carbon dioxide electrolysers. Nat Energy [Internet]. 2021 [cited 2025 Nov 3];6(4):439–48. Available from: https://www.nature.com/articles/s41560-021-00813-w

10. Hao S, Elgazzar A, Ravi N, Wi TU, Zhu P, Feng Y, Xia Y, Chen FY, Shan X, Wang H. Improving the operational stability of electrochemical CO2 reduction reaction via salt precipitation understanding and management. Nat Energy [Internet]. 2025 [cited 2025 Nov 3];10(2):266–77. Available from: https://www.nature.com/articles/s41560-024-01695-4

11. Disch J, Ingenhoven S, Vierrath S. Bipolar Membrane with Porous Anion Exchange Layer for Efficient and Long-Term Stable Electrochemical Reduction of CO2 to CO. Adv. Energy Mater [Internet]. 2023 [cited 2025 Nov 3];13(38):2301614. Available from: https://onlinelibrary.wiley.com/doi/abs/10.1002/aenm.202301614

12. Haas T, Krause R, Weber R, Demler M, Schmid G. Technical photosynthesis involving CO2 electrolysis and fermentation. Nat Catal [Internet]. 2018 [cited 2025 Nov 3];1(1):32–9. Available from: https://www.nature.com/articles/s41929-017-0005-1

13. Lim C, Kim S, Song JH, Han MH, Ko YJ, Lee KY, Choi JY, Lee WH, Oh HS. Breaking the current limitation of electrochemical CO 2 reduction via a silica-hydroxide cycle. Energy Environ Sci [Internet]. 2024 [cited 2025 Nov 3] ;17(17):6215-24. Available from: https://pubs.rsc.org/en/content/articlehtml/2024/ee/d4ee00448e

14. Bard AJ, Faulkner LR, White HS. Electrochemical methods: fundamentals and applications [Internet]. John Wiley & Sons; 2022 [cited 2026 Mar 31]. Available from: https://books.google.com/books?hl=en&lr=&id=4ShuEAAAQBAJ&oi=fnd&pg=PR21&dq=Bard,+A.+J.,+Faulkner,+L.+R.,+%26+White,+H.+S.+(2022).+Electrochemical+methods:+fundamentals+and+applications.+John+Wiley+%26+Sons&ots=SJHuzXVzwC&sig=fBqI7gEe7aE0y9e-OkZMEn0u2jQ

15. O'Brien CP, Miao RK, Shayesteh Zeraati A, Lee G, Sargent EH, Sinton D. CO_2 Electrolyzers. Chem Rev [Internet]. 2024 [cited 2026 Mar 31];124(7):3648–93. Available from: https://pubs.acs.org/doi/10.1021/acs.chemrev.3c00206

16. Burdyny T, Smith WA. CO 2 reduction on gas-diffusion electrodes and why catalytic performance must be assessed at commercially-relevant conditions. Energy Environ Sci [Internet]. 2019 [cited 2026 Mar 31];12(5):1442–53. Available from: https://pubs.rsc.org/en/content/articlehtml/2011/xw/c8ee03134g

17. Xu Y, Edwards JP, Zhong J, O'Brien CP, Gabardo CM, McCallum C, Li J, Dinh CT, Sargent EH, Sinton D. Oxygen-tolerant electroproduction of C 2 products from simulated flue gas. Energy Environ Sci [Internet]. 2020 [cited 2026 Mar 31];13(2):554–61. Available from: https://pubs.rsc.org/en/content/articlehtml/2020/ee/c9ee03077h

18. Yoon W, Weber AZ. Modeling low-platinum-loading effects in fuel-cell catalyst layers. J. Electrochem. Soc [Internet]. 2011 [cited 2026 Mar 31];158(8):B1007–18. Available from: https://iopscience.iop.org/article/10.1149/1.3597644/meta

19. Van Allsburg KM, Tan EC, Super JD, Schaidle JA, Baddour FG. Early-stage evaluation of catalyst manufacturing cost and environmental impact using CatCost. Nat. Catal [Internet]. 2022 [cited 2025 Jul 28];5(4):342–53. Available from: https://idp.nature.com/authorize/casa?redirect_uri=https://www.nature.com/articles/s41929-022-00759-6&casa_token=KjmnXeUsqPIAAAAA:_J4fCCorW3FtTTmGvEyHDmAJnAY97g5nNI9g4NkSqj0y3Pbk2oJHRNli3ev65G0Ri7NLVEuCi3a99U1X6vQ

20. Anekwe IM, Lora EE, Subramanian KA, Kozlov A, Zhang S, Oboirien B, Isa YM. Techno-economic and life-cycle analysis of single-step catalytic conversion of bioethanol to fuel blendstocks over Ni-doped HZSM-5 zeolite catalyst. Energy Convers. Manag.: X [Internet]. 2024 [cited 2025 Jul 28];22:100529. Available from: https://www.sciencedirect.com/science/article/pii/S2590174524000072